Article

Operando formation of highly efficient electrocatalysts induced by heteroatom leaching

Cong Liu [1,2], Bingbao Mei[3], Zhaoping Shi[1,2], Zheng Jiang [2,3], Junjie Ge[1], Wei Xing [1,2], Ping Song [1] ✉ & Weilin Xu [1,2] ✉

Heterogeneous nano-electrocatalysts doped with nonmetal atoms have been studied extensively based on the so-called dopant-based active sites, while little attention has been paid to the stability of these dopants under working conditions. In this work, we reveal significantly, when the redox working potential is too low negatively or too high positively, the active sites based on these dopants actually tend to collapse. It means that some previously observed "remarkable catalytic performance" actually originated from some unknown active sites formed in situ. Take the Bi-F for the CO_2RR as an example, results show that the observed remarkable activity and stability were not directly from F-based active sites, but the defective Bi sites formed in situ after the dopant leaching. Such a fact is unveiled from several heteroatom-doped nanocatalysts for four typical reactions (CO_2RR, HER, ORR, and OER). This work provides insight into the role of dopants in electrocatalysis.

Nonmetal (N, F, S, etc.)-doped heterogeneous nanocatalysts have been extensively studied for energy-related electrochemical reactions, such as electrochemical CO_2 reduction reaction (CO_2RR)[1–5], hydrogen evolution reaction (HER)[6,7], oxygen reduction reaction (ORR)[8–10] and oxygen evolution reaction (OER)[11,12]. Nonmetal dopant-based active sites have been taken simply as the main contributors for the high performance of nanocatalysts, due to the boosting activity after doping[13–16]. All the explanations or density functional theory (DFT) calculations about the enhanced catalytic performances were directly based on the heteroatom-based active sites[17–20]. While due to the known limited stability of these nonmetal dopants on supports[21–23], deep understanding to the real roles of these doped heteroatoms under working conditions is highly desirable for the energy-related electrochemical industry[24–28]. While by now little has been done to reveal the working mechanisms of these nonmetal dopants under working conditions[29,30]. For instance, it is still not clear about the potential-dependent stability of dopants during the redox processes, such as CO_2RR, HER, ORR, and OER[31–36].

In this work, based on a fluorinated bismuth oxide (Bi_2O_3-F) with high CO_2RR performance for the production of formate, besides the expected extremely fast reduction of Bi_2O_3-F to metallic Bi-F in seconds, we surprisingly observed the fast leaching of doped F from Bi support in minutes to form defective Bi in situ. It means that the observed high activity and stability of CO_2RR performance of "Bi-F" doesn't originate directly from the F-based active sites, but the defective Bi sites formed in-situ after the leaching of F. Such fact was further confirmed by DFT calculations. The fast leaching of heteroatom-dopants was further observed on F, N-doped carbon surfaces during CO_2RR/HER/OER processes. While as for the ORR process on F, N-doped carbon surfaces, it shows that the F- and N-dopants are very stable in the typical ORR potential window, which is not too far from the relative hydrogen electrode (RHE). All these results indicate that the observed high performances of the nonmetal heteroatoms-doped electrocatalysts for the redox process at too high positive or too low negative potentials are usually not from the dopants directly but from the sites formed in-situ after the leaching of these

[1]State Key Laboratory of Electroanalytical Chemistry, & Jilin Province Key Laboratory of Low Carbon Chemical Power, Changchun Institute of Applied Chemistry, Chinese Academy of Sciences, Changchun 130022, China. [2]School of Applied Chemistry and Engineering, University of Science and Technology of China, Hefei 230026, China. [3]Shanghai Synchrotron Radiation Facility, Shanghai Institute of Applied Physics, Chinese Academy of Sciences, Shanghai 201204, China. ✉e-mail: songping@ciac.ac.cn; weilinxu@ciac.ac.cn

heteroatoms. It means that the conclusions made in previous work especially that for CO$_2$RR, HER, and OER need to be reconsidered. This work provides insight into the real role of heteroatoms doped and the real activity origin of nonmetal-doped materials under working conditions and offers a protocol to engineer highly efficient active sites with respect to dopant leaching process.

Results and discussion

We firstly prepared pure bismuth oxide nanoparticles (Bi$_2$O$_3$) and fluorinated bismuth oxide nanoparticles (Bi$_2$O$_3$-F) via the air annealing process based on the precursor bismuth nanoparticles (Pre Bi) and NaF (see details in the Methods). The scanning electron microscopy (SEM) images for Bi$_2$O$_3$ and Bi$_2$O$_3$-F indicate that the air annealing does not change the morphology of Pre Bi (Fig. 1a, c and Supplementary Fig. 1). The high-resolution transmission electron microscope (HRTEM) analysis indicates that the lattice spacing of (221)-facet of Bi$_2$O$_3$-F is slightly larger than that of Bi$_2$O$_3$ (Fig. 1b, d), consistent with the X-ray powder diffraction (XRD) results shown in Supplementary Fig. 1. Such facts indicate that the F-doping can tune the lattice structure of Bi$_2$O$_3$ via the formation of Bi-F bonding (Supplementary Fig. 2, Supplementary Table 1)[37]. The CO$_2$RR performance of both Bi$_2$O$_3$ and Bi$_2$O$_3$-F were evaluated by determining the Faradaic efficiency (FE) of products with

online-connected gas chromatograph and ^{1}H-NMR spectra (Supplementary Figs. 3 and 4). As shown in Fig. 1e, f, compared with Bi$_2$O$_3$, Bi$_2$O$_3$-F presents much higher Faradaic efficiencies for the HCOO$^-$ production (FE$_{HCOO^-}$) in a wide potential range (−0.77 V to −1.27 V vs. RHE). Partial current densities for HCOO$^-$ (j_{HCOO^-}) confirm the higher catalytic performance of Bi$_2$O$_3$-F than Bi$_2$O$_3$ (Fig. 1g, Supplementary Fig. 5, Supplementary Fig. 6, and Supplementary Table 2). We further studied the CO$_2$RR stabilities of catalytic performance of both Bi$_2$O$_3$ and Bi$_2$O$_3$-F (Supplementary Fig. 7). As shown in Fig. 1h, after a long-term (100 hours) continuous CO$_2$RR process, the FE$_{HCOO^-}$ on Bi$_2$O$_3$-F decreased only 11%, while the FE$_{HCOO^-}$ on Bi$_2$O$_3$ decreased up to 22%, indicating a much higher stability of Bi$_2$O$_3$-F than Bi$_2$O$_3$ for the formate production from CO$_2$RR. Such improvement obviously originates from the doping of F. To here, All these results indicate that the F doping indeed can improve the CO$_2$RR catalytic performance of Bi$_2$O$_3$, consistent with previous observations about the performance enhancement of electrocatalysts by the doping of non-metal atoms on supports[35].

To further understand the role of F or catalytic mechanism of F-based active sites, we first investigate the possible component variation of the catalyst during the CO$_2$RR process. Operando Raman spectra (Fig. 2a and Supplementary Fig. 8) show firmly that the Bi$_2$O$_3$
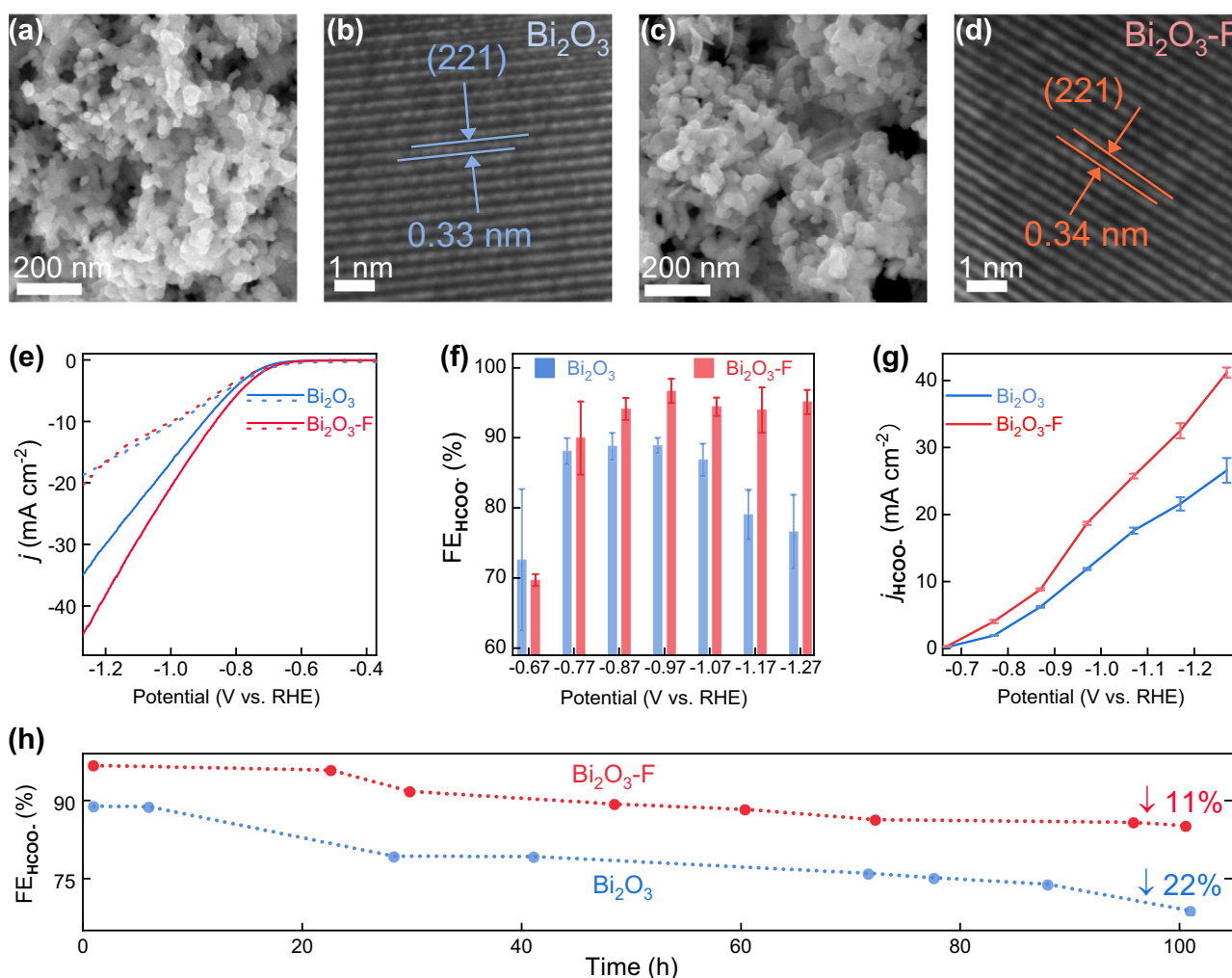

Fig. 1 | Structural and electrochemical properties. a SEM and **b** HRTEM images of Bi$_2$O$_3$. **c** SEM and **d** HRTEM images of Bi$_2$O$_3$-F. Lattice spacing is represented by the blue and red mark. **a**, **c** Scale bar = 200 nm; **b**, **d** Scale bar = 1 nm. **e** Comparison of linear sweep voltammetric (LSV) with pH corrections for CO$_2$ (solid line, pH 7.2) and Ar (dash line, pH 8.8) saturated electrolytes. Colors in blue and red represent Bi$_2$O$_3$ and Bi$_2$O$_3$-F, respectively. **f** Comparison of FE$_{HCOO^-}$ at different applied potentials ranging from −0.67 V to −1.27 V (RHE). Error bars correspond to the standard deviation of three independent measurements. **g** Comparison of j_{HCOO^-} at different applied potentials ranging from −0.67 V to −1.27 V (RHE). **h** Long-term durability of formate selectivity of the Bi$_2$O$_3$ (blue), and Bi$_2$O$_3$-F (red) under chronoamperometry test (−0.97 V vs. RHE, 0.5 M KHCO$_3$).
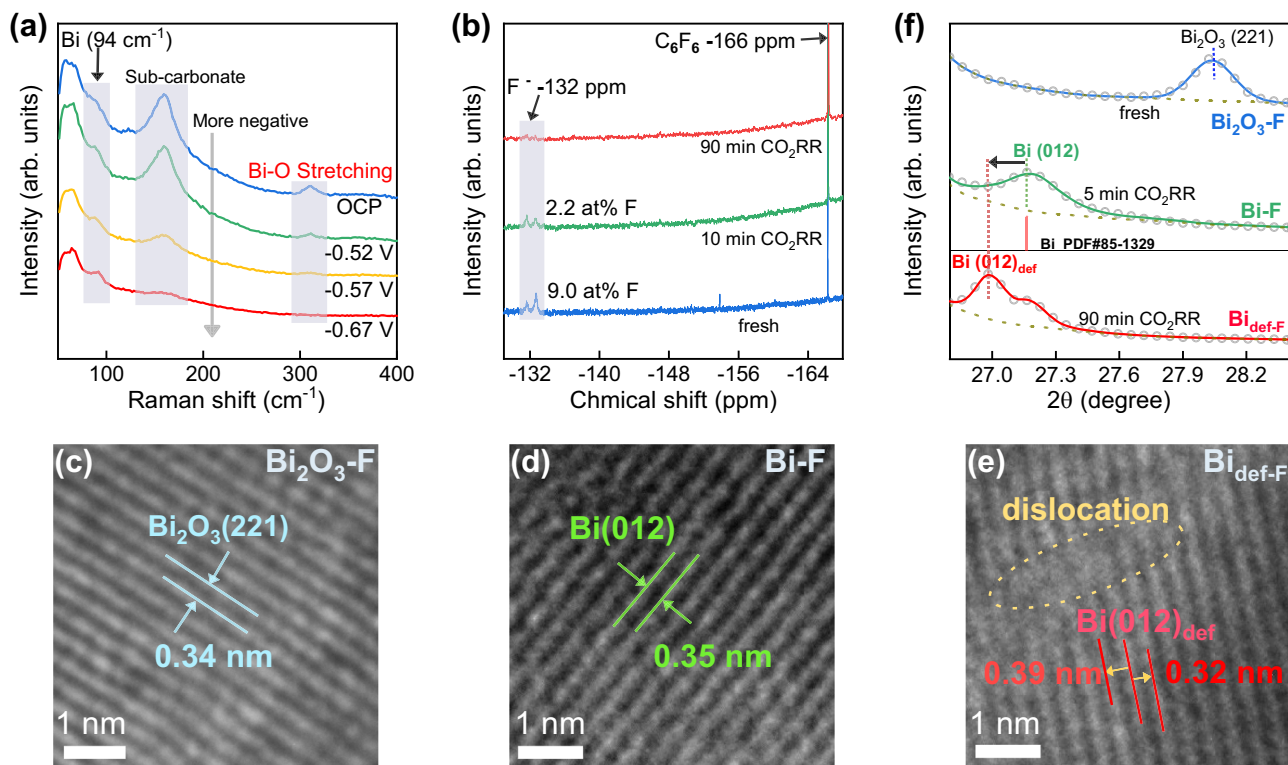
Fig. 2 | Structural evolution of Bi₂O₃-F during CO₂RR. a Operando Raman spectra of Bi₂O₃-F during CO₂RR process in the potential range from −0.52 V to −0.67 V vs. RHE in CO₂ saturated 0.5 M KHCO₃. The sweep duration for each potential is 30 seconds. **b** Time-dependent ¹⁹F-NMR spectra of Bi₂O₃-F after CO₂RR at -0.97 V. HRTEM images of **c** fresh Bi₂O₃-F, **d** Bi-F and **e** Bi$_{def-F}$ (note: Bi-F and Bi$_{def-F}$ are derived from the fresh Bi₂O₃-F after 5 min and 90 min CO₂RR, respectively). Scale bar = 1 nm. **f** The Rietveld-refined XRD results of Bi₂O₃-F, Bi-F, and Bi$_{def-F}$. Colors in blue, green, and red represent Bi₂O₃-F, Bi-F, and Bi₂O₃-F, respectively.

can be reduced fast to metallic Bi in seconds under the potential for CO₂RR as indicated by the fast disappearance of Bi-O stretch peaks (312 cm⁻¹) and the appearance of a peak for metallic Bi (94 cm⁻¹)[38,39]. Such fact means that the real components for long-term CO₂RR process observed above is from Bi or Bi-F rather than the original Bi₂O₃ or Bi₂O₃-F. To further unveil the status of dopants in Bi₂O₃-F during the CO₂RR process, the fluoride species on Bi₂O₃-F were investigated by ¹⁹F-NMR spectra after certain time of CO₂RR at -0.97 V (Supplementary Fig. 9). Surprisingly, Fig. 2b shows, after 10 minutes of CO₂RR, the fluorine content on Bi₂O₃-F dropped hugely from 9.0at% to 2.2at% and the fluorine almost disappears after 90 minutes. The above facts mean that two sequential reconstructions occur quickly on Bi₂O₃-F during the CO₂RR process: the first is the fast reduction from Bi₂O₃-F to F-doped metal (Bi-F) in seconds, the second is the leaching of F to produce defective Bi surface (Bi$_{def-F}$) in minutes. So, the long-term CO₂RR actually mainly occurs on Bi$_{def-F}$. From the performance shown in Fig. 1, one can tell that the defective Bi surface (Bi$_{def-F}$) possesses much higher CO₂RR activity and stability than pure smooth Bi surface.

We next conducted the lattice analysis on the above three catalysts (including fresh Bi₂O₃-F) to gain more insights. The analyzes of the HRTEM (Fig. 2c−e) show that the reduction of Bi₂O₃-F can increase slightly the lattice distance (from 0.34 nm to 0.35 nm) and the further leaching of F enables the local dislocation as indicated by the simultaneous appearance of both larger (from 0.35 nm to 0.39 nm) and smaller (from 0.35 nm to 0.32 nm) lattice distances. Such a unique defect feature observed on Bi$_{def-F}$ surface cannot be found on the surface of reduced Bi₂O₃ (Supplementary Fig. 10), confirming such unique feature originates in situ from the F leaching. The XRD patterns (Fig. 2f, Supplementary Fig. 11, and Supplementary Table 3) further unveil a new facet of defective Bi(012) formed-in situ after the F leaching as indicated by the peak at 27.0 degrees observed on Bi$_{def-F}$, indicating that the Bi$_{def-F}$ undergoes lattice expansion after the F

leaching[40]. To here, one can conclude that the leaching of F atoms from Bi surface induces the local dislocation and then the in-situ formation of defective sites by removing some Bi atoms along with.

We further did the density functional theory (DFT) calculation to understand the activity origin of Bi-F and Bi$_{def-F}$ for CO₂RR. Firstly, based on the above experimental results, we constructed the metallic Bi (hexagonal, Bi(012)), one fluorine atom modified metallic Bi (Bi(012)-F), and defective Bi(012) (Bi(012)$_{def-F}$, in-situ formed defective sites after F-leaching from Bi(012)-F). Optimized geometric structures can be found in Supplementary Fig. 12. Notably, after the F-leaching, the formed defective sites enable the change of geometric structures of the neighbor Bi atom (Fig. 3a), which is in good agreement with the outcomes in Fig. 2c−e. To gain more insights into these three catalytic surfaces, the electron localization function (ELF) was calculated to measure the degree of electronic localization (the probability of finding an same spin electron in the nearby space)[41]. As shown in Fig. 3b, the Bi(012)$_{def-F}$ displays higher electron delocalization around the formed defective sites than that on Bi(012) and Bi(012)-F. Correspondingly, the detailed projected density of states (PDOS) reveals that the electron density near the Fermi level (E$_f$) became higher in Bi(012)$_{def-F}$ surface (Supplementary Fig. 13), which could give rise to the more efficient surface electron transfer[42]. The above results confirm that the electronic structure of Bi(012)$_{def-F}$ surface was changed after defective sites formed due to the leaching, which can further affect positively the CO₂RR catalytic activity.

For the formate production on these Bi-based catalysts, the formation of *OCHO intermediate was considered as the primary pathway[43–45]. Therefore, we calculated the adsorption energies of *OCHO on these three catalytic surfaces: Bi(012), Bi(012)-F, and Bi(012)$_{def-F}$ (Supplementary Fig. 14). DFT calculations show that the adsorption energies of *OCHO are −1.3, −1.2, and −1.9 eV on them, respectively (Fig. 3c). We further calculated the Gibbs free energy (ΔG)
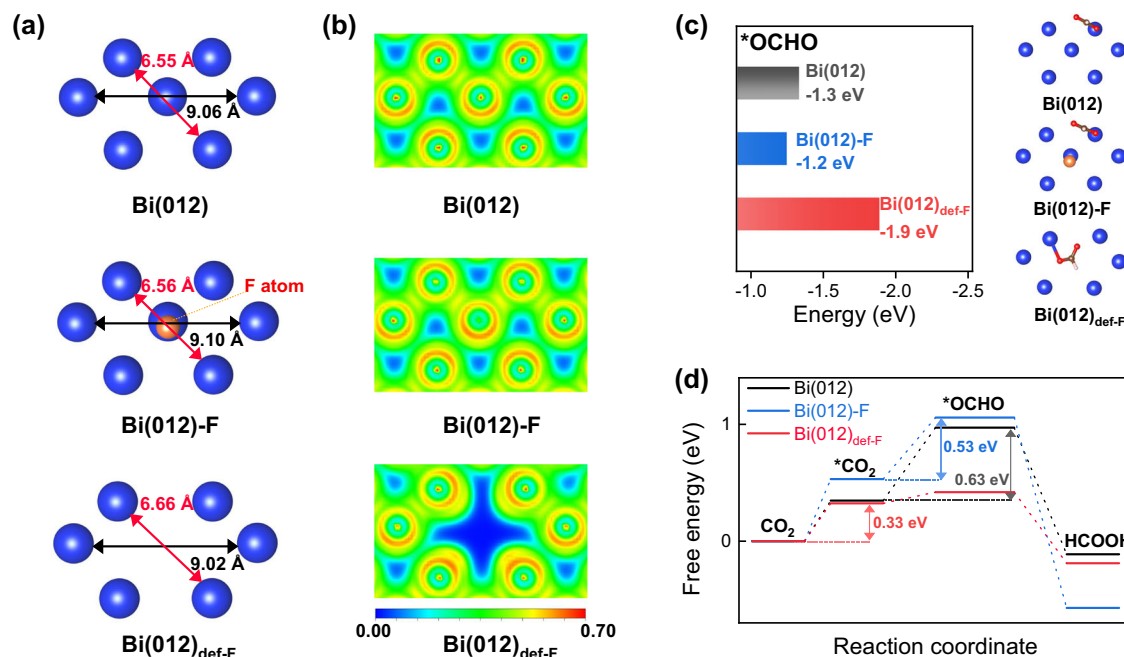
Fig. 3 | Theoretical calculations. a The partial slice of optimized geometric structures (Bi(012), Bi(012)-F, and Bi(012)$_{def\text{-}F}$). The introduction of a dopant atom (F, orange color) enables the change of distance between the neighbor Bi atoms. b Comparison of electron localization function calculated from the optimized geometric structures. c Comparison of the binding energy of *OCHO in the different catalytic surfaces. Colors in grey, blue, and red represent Bi(012), Bi(012)-F, and Bi(012)$_{def\text{-}F}$, respectively. Right: The corresponding adsorption structures of *OCHO. d Free energy profiles for the formation of *OCHO intermediate on the catalytic surface of Bi(012), Bi(012)-F, and Bi(012)$_{def\text{-}F}$.

for the *OCHO formation (0.63, 0.53, and 0.09 eV respectively, Fig. 3d). These results reveal that the defective sites facilitate the formation of *OCHO. More importantly, after the leaching of dopant atoms, the reaction barrier of the rate-limiting step in the Bi$_{def\text{-}F}$ surface further decreases to 0.33 eV (lower than Bi(012) and Bi(012)-F), indicating that the observed much higher CO_2RR performance of Bi_2O_3-F (Fig. 1) should be attributed to the defective sites formed in situ after the F leaching. We further calculated the charge density difference and the electron transfer (bader charge) on these three intermediate-adsorbed catalytic surfaces: Bi(012), Bi(012)-F, and Bi(012)$_{def\text{-}F}$. As shown in Supplementary Fig. 15, the F doping can weaken the electron transfer from Bi to O and then weaken the adsorption of the intermediate on Bi, while after the formation of defects via the leaching of F, the electron transfer from Bi to O can be enhanced, which then enhances the adsorption of the intermediate on Bi.

In addition, based on the experimental results shown in Fig. 2e, f about the F-leaching induced lattice expansion, we further studied its effect on the CO_2RR performance of Bi. The results (Supplementary Fig. 16 and Supplementary Note 1) showed that such lattice expansion can improve slightly its catalytic activity for CO_2RR via a rate-limiting step of CO_2 activation.

Since heterogeneous nano-electrocatalysts doped with nonmetal atoms have been studied extensively for all kinds of redox reactions in a wide potential range[46–48], it is very necessary to further confirm the universality of above unveiled in-situ formation of active sites via the leaching of dopants on heterogeneous nanocatalysts. For this goal, we fabricated F- and N- doped carbon black based on BLACK PEARLS (BP) (BP-F and BP-N, Supplementary Fig. 17 and Supplementary Fig. 18) to gain more insights into the stability of typical dopants of F and N in a much wider potential range. Based on the standard electrode potentials of half-electrochemical thermodynamic reaction (Supplementary Table 4), we choose to study the four most typical and important energy chemistry processes (CO_2RR, HER, ORR, and OER) covering the electrode potential from −1.0 V to 1.8 V vs. RHE. As shown in Fig. 4a, with potential lower than −0.5 V in CO_2-saturated 0.5 M $KHCO_3$, BP-F

and BP-N exhibit catalytic activity for CO_2RR to produce CO (Supplementary Fig. 19 and Supplementary Fig. 20). In the potential range between −0.7 V and 1.0 V, BP-F and BP-N exhibited remarkable HER and ORR activities (Fig. 4b). At much higher positive potentials (> 1.0 V), BP-F and BP-N also present OER activities. Based on such facts, BP-F and BP-N are taken as model catalysts to validate the dopant stability under different test intervals.

The typical ex-situ XPS analysis (Fig. 4c, d) shows that the F- and N-dopants were rapidly removed at negative reduction potential when during the CO_2RR (-0.87 V vs. RHE) while still maintained steadily when during the ORR at 0 V vs. RHE. Based on such qualitative analysis, the leaching processes of both F and N doped on carbon were analyzed deeply for the catalytic processes of CO_2RR, HER, ORR, and OER, respectively. As shown in Fig. 4e, g, at more negative potentials such as -0.87 V and −0.67 V for CO_2RR, the F- and N-dopants leached rapidly, while the sustained high catalytic activities of these two catalysts in a long-time testing window (Supplementary Fig. 21) indicate that the observed long-term activities originate from defects formed after the dopant leaching (Supplementary Figs. 22 and 23). With the potential increase up to -0.37 V and -0.47 V for HER (Fig. 4e, g), the leaching rates of both F- and N-dopants decrease a little bit. Moreover, the catalytic activity of HER in BP-F increased after the dopant leaching, suggesting the long-term HER activity of BP-F is also from the active sites formed in situ (Supplementary Fig. 24). With the potential further increase up to 0.0 V, 0.3 V, and 0.6 V for ORR (Fig. 4e, g), the heteroatoms of F and N were stable in the potential window for ORR, implying that the doped heteroatoms on support indeed are the main contributors for the long-term ORR process (Supplementary Fig. 25). While at much higher positive potentials for such as OER (1.5 V and 1.8 V), the leaching occurs fast again (Fig. 4e, g). Figure 4f, h summarizes the leaching rates of dopants (F and N) at different test intervals, clearly elucidating the potential dependent leaching of dopants.

To further validate whether such leaching is related to the catalytic reaction or not, we conducted control experiments with these two catalysts in Ar-saturated 0.5 M $KHCO_3$ at -0.87 V. Supplementary
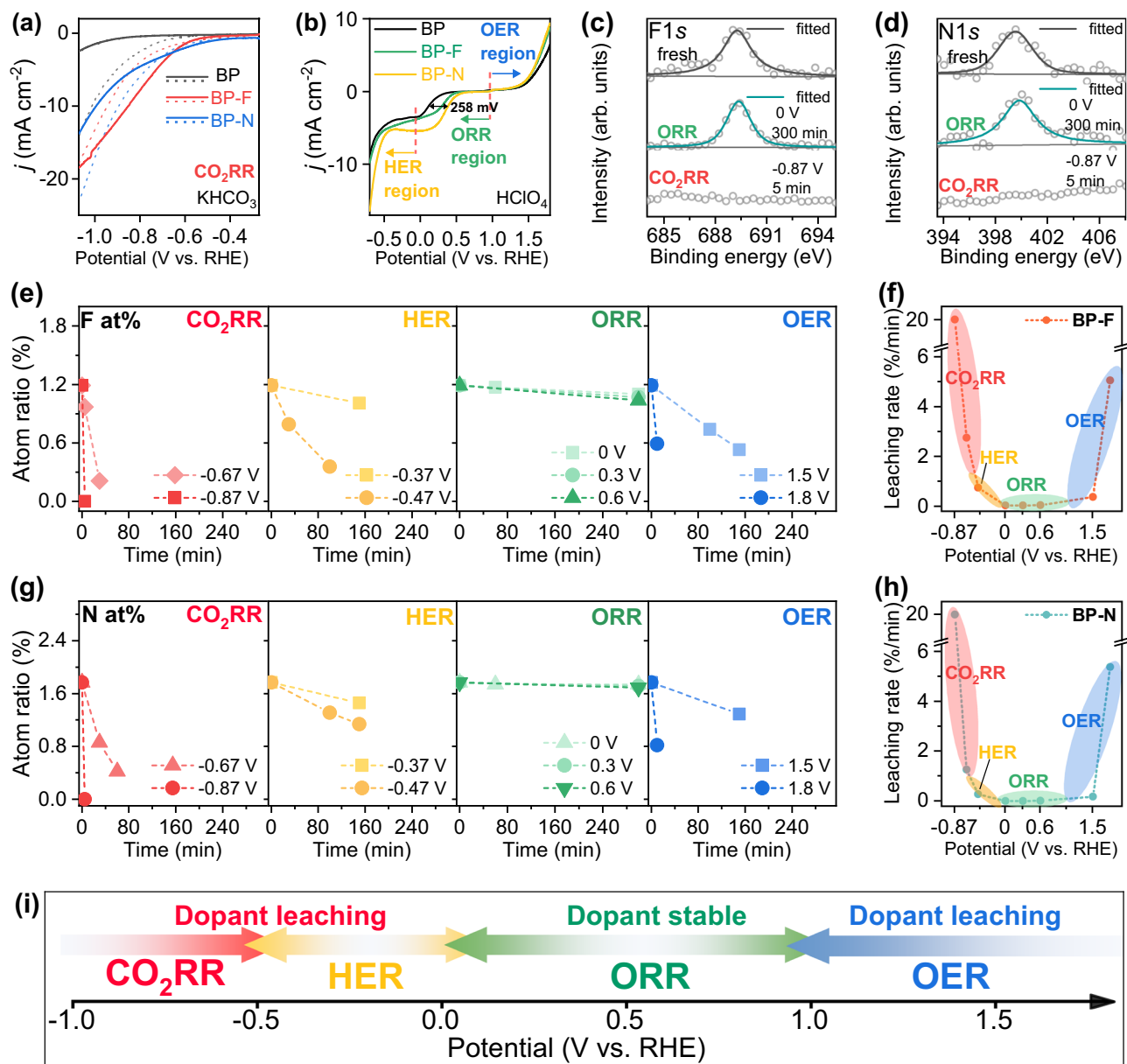
Fig. 4 | Potential-driven dopant leaching in different materials. a Comparison of LSV with pH corrections for CO_2 (solid line, pH 7.2) and Ar (dash line, pH 8.8) saturated electrolytes (0.5 M $KHCO_3$). Colors in black, red, and blue represent BP, BP-F, and BP-N, respectively. **b** The linear sweep curves of the catalyst were tested in O_2-saturated 0.1 M $HClO_4$ (rotation rate 1600 rpm, scan rate of 5 mV s^{-1}). The test interval is divided into three range areas: OER, ORR, and HER regions. Colors in black, green, and yellow represent BP, BP-F, and BP-N, respectively. **c** F1s XPS of BP-F and **d** N1s XPS of BP-N after 5 min CO_2RR (-0.87 V vs. RHE) and 300 min ORR (0 V vs. RHE). **e** F-dopant content and (**g**) N-dopant content as a function of potential applied time in the CO_2RR, HER, ORR, and OER. The ORR and OER were tested in O_2-saturated 0.1 M $HClO_4$, HER was tested in Ar-saturated 0.1 M $HClO_4$, and CO_2RR was tested in CO_2-saturated 0.5 M $KHCO_3$. **f** F-dopant and **h** N-dopant leaching rates as a function of potential applied. The leaching rates of dopants in the specific voltage (unit: %/min) is based on the leaching degree divided by the leaching time. **i** The schematic diagram of dopant leaching (BP-F and BP-N) in the corresponding electrochemical processes.

Fig. 26 shows clearly that the leaching rates of both F and N are the same as that observed during the CO_2RR process at the same potential, indicating that the leaching is mainly driven by the electrode potential rather than the redox reaction. We studied the dopant-dependent leaching rates at the same potential (Supplementary Fig. 27) and found that the leaching of F is slightly faster than N from carbon surface probably due to the different binding structures of C-F and C-N[49,50]. Considering the different electrochemical reaction conditions that have appeared in previous studies[35,51–54], we also compared the dopant leaching in the different type of electrolytes (Supplementary Figs. 28 and 29), and different types of host material (Supplementary Fig. 30). Based on the above control experiments, we further conclude that the

dopant leaching rates are related to the type of electrolyte, dopant atom, or host material, but the leaching mechanism is same: the driving force of leaching is the voltage.

To further confirm the leaching window and stable window of dopants N and F from a theoretical perspective, we calculated the surface Pourbaix diagram to unfold the operando surface condition. As shown in Supplementary Fig. 31[55–57], the obtained leaching Pourbaix diagram reveals that the F- and N-dopants leach at either too high or too low potential ranges while a relatively stable potential interval exists in the middle range of the voltage, which is in good agreement with the experimental outcomes (Fig. 4). Based on the above facts, the stabilities of dopant atoms (mainly F, N studied here) in the different

electrochemical processes were summarized in Fig. 4i. The potential-induced leaching mechanism of dopants (F and N) or in-situ formation of active sites via the leaching of dopants revealed here inspire us to rethink the design and the activity origin of dopant-induced highly efficient nanocatalysts.

In summary, we studied the stability of dopants on heterogeneous nano electrocatalysts for the four most representative and important redox reactions under working conditions. It reveals significantly that the active sites based on these dopants actually can collapse due to the fast leaching of dopants when the redox working potential is too low or too high. It means that some previously observed "remarkable catalytic activity and stability" actually originated from the active sites formed in situ. Such a fact is unveiled from several heteroatom-doped nanocatalysts (Bi-F, C-F, and C-N) for CO_2RR, HER, ORR, and OER, respectively. Take the Bi-F for the electrocatalytic CO_2RR to produce formate as an example, results show that the observed remarkable activity and stability is not directly from F-based active sites, but the defective Bi sites formed in situ after the fast leaching of F at negative potentials. Similar results are observed on F, N-doped carbon (BP-F and BP-N) in the potential window for CO_2RR and HER, respectively. While during the ORR process on BP-F and BP-N, the dopants are stable. At more positive potentials such as for OER process, the fast leaching of dopants occurs again. The work provides insight into the real role of heteroatoms doped on nanocomposites for electrocatalysis and a protocol for the in-situ formation of highly efficient active sites on functional materials via the leaching of dopants.

Methods

Materials
Bismuth (III) chloride was purchased from adamas-beta, China; Polyethene glycol (Mn 1000), hydrochloric acid (HCl, 30 wt%) and ethanol were purchased from Xilong scientific, China; 2-ethoxyethanol, sodium fluoride (NaF), ammonium fluoride (NH_4F), melamine ($C_3H_6N_6$), tetradecylamine (TDA), tin tetrachloride ($SnCl_4$), potassium bicarbonate ($KHCO_3$), Deuterium oxide (D_2O, 99.9%) and hexafluorobenzene (C_6F_6, 99.9%) were purchased from Aladdin, China; Dimethyl sulfoxide (DMSO, 99.99%) and Nafion solutions (5 wt%) were purchased from Sigma-Aldrich. Carbon black (BLACK PEARLS 2000, noted as BP) was purchased from Cabot, America. All chemicals were used without further purification. The resistivity of deionized water was 18.2 MΩ cm in solution preparations.

Preparation of precursor bismuth nanoparticles (Pre Bi)
Bismuth (III) chloride (100 mg), polyethene glycol (1.2 g) were dissolved into 60 mL 2-ethoxyethanol, then the sample was under ultrasonication to form a uniform and transparent solution. The solution of $NaBH_4$ (10 mL, 60 mmol) was used to reduce the bismuth (III) chloride. After twice washing with water and ethanol the mixture was collected by filtration. Finally, the sample was dried in a vacuum oven at 50 °C and then collected for further experiments.

Preparation of bismuth oxide nanoparticles (Bi_2O_3, Bi_2O_3-F)
Pre Bi (10 mg) was mixed with a certain amount of NaF (0 mg and 1.6 mg) and annealed at 200 °C in the air for 6 h to obtain bismuth oxide or fluorinated bismuth oxide nanoparticles (Bi_2O_3 and Bi_2O_3-F). After washing with enough water, the sample was dried in a vacuum oven at 50 °C and then collected for further experiments.

Preparation of F-doped carbon (BP-F)
Carbon black (BP) was mixed with a certain amount NH_4F (30 wt%), then the mixture was dispersed in 50% ethanol solution. After fiercely stirring, the mixture was dried under a vacuum at 50 °C and then pyrolyzed at 400 °C under argon atmosphere for 6 h with a flow rate of 80 mL min⁻¹. After washing with enough water, the sample was dried in a vacuum oven at 50 °C and then collected for further experiments.

Preparation of N-doped carbon (BP-N)
Carbon black (BP) was mixed with a certain amount of melamine (mass ratio 1:15). After repeated grinding, the mixture was pyrolyzed at 900 °C under argon atmosphere for 1 h with a flow rate of 80 mL min⁻¹. After washing with enough water, the sample was dried in a vacuum oven at 50 °C and then collected for further experiments.

Preparation of fluorinated tin oxide (SnO_2-F)
The synthesis method was derived from ref. 35,58. $SnCl_4$ (2.61 g) and NH_4F (0.374 g) were mixed in TDA solution (1.28 g TDA, 85 mL ethanol, and 160 mL deionized water). The ammonium hydroxide solution (1.5 mmol L⁻¹, 200 mL) was added dropwise, followed by stirring for 1 h. Then the suspension was refluxed at 80 °C for 72 h. After cooling to room temperature and ethanol washing, the mixture was hydrothermally treated at 120 °C for 24 h. After the hydrothermal process, the sample was washed with adequate ethanol and dried in a freeze dryer. Finally, the drying sample was calcined at 400 °C in the air for 3 h and then collected for further experiments.

Structural characterizations
The morphology was characterized by scanning electron microscopy (SEM, ZEISS Sigma-300) and transmission electron microscopy (TEM, JEOL JEM-2100, 200 kV). The basic physical structure was characterized by X-ray diffraction (XRD, Rigaku-D/MAX-PC 2500, Cu Kα source), confocal Raman spectroscopy (Horiba-JY Labram-010, 532 nm Nd laser), and X-ray photoelectron spectroscopy (XPS, Thermo ESCALAB 250, Al Kα source). ¹H-NMR and ¹⁹F-NMR were performed on a BRUKER ADVANCE-III 500HD (Switzerland). X-ray absorption spectras (XAS) were performed on the BL14W1 beamline at the Shanghai Synchrotron Radiation Facility (SSRF). Electrochemical data were collected by electrochemical work station (CH Instruments, CHI 760E).

Electrochemical measurements in a three-electrode cell
The HER, ORR, and OER performance was tested by Pine Modulated Speed Rotator (PINE, America). 1 mg samples, 10 μL Nafion solutions (5 wt%), and 200 μL ethanol were mixed and dispersed by ultrasonication to form catalyst ink. 10 μL ink was evenly drop-cast onto the surface of the rotating disk electrode (RDE) to work as working electrode. A carbon rod and Ag/AgCl reference electrode (3.5 M KCl aqueous used as the filling solution) were used as the counter and reference electrode, respectively. The HER, ORR, and OER performance were determined by linear sweep curves test (LSV) in Ar/O_2 saturated electrolytes (scan rate: 5 mV s⁻¹).

Electrochemical CO_2 reduction
The detection of typical CO_2RR product was performed with an H-type two-compartment electrochemical cell (H-cell). Cation-exchange membrane (Nafion 117, Dupant Company) was used to separate working and counter electrodes (cathodic and anodic compartments). 210 μL ink (1 mg catalysts) was evenly drop-cast onto the surface of carbon paper (1×1 cm²) as a working electrode. Electrode potentials (Ag/AgCl) were converted to potentials versus the reversible hydrogen electrode (RHE) by:

$$E_{RHE} = E_{Ag/AgCl} + 0.0591 \times pH + 0.205 \qquad (1)$$

Before the experiments, the electrolyte (50 ml 0.5 M $KHCO_3$) was saturated with CO_2 (50 mL min⁻¹) at least 30 min at room temperature and ambient pressure. Gas chromatograph (GC, Thermo Trace 1300) was online-connected with the H-cell, with a Molecular Sieve 5 A capillary column and a packed Carboxen-10000 column. Helium (99.999%, Juyang Co. Ltd.) was used as the GC carrier gas. Hydrogen and carbon monoxide were quantified by thermal conductivity and flame ionization detector (TCD, FID, equipped with a methanizer), respectively. The Faradaic efficiency (FE) and the partial current

densities of gas products (H_2,CO) were calculated as below:

$$FE_S = \frac{2Fv_s GP_0}{RT_0 i_{total}} \times 100\% \quad (2)$$

$$j_{H_2} = \frac{FE_{H_2} \times i_{total}}{electrode\ area} \quad (3)$$

$$j_{CO} = \frac{FE_{CO} \times i_{total}}{electrode\ area} \quad (4)$$

Where V_s represents hydrogen and carbon monoxide volume concentrations from the exhaust gas of H-cell (GC quantified), $P_0 = 1.013$ bar and $T_0 = 298.15$ K, G represents gas flow rate (mL min^{-1}, exit of cathodic compartment), i_{total} represents steady-state cell current (mA), F = 96485 C mol^{-1}, R = 8.314 J mol^{-1} K^{-1}.

Liquid product was quantified by ^{1}H-NMR spectra. Typical NMR samples were mixed by 500 μL electrolyte, 100 μL D_2O, and 0.05 μL DMSO (internal standard). The FE can be calculated as follows:

$$FE_{HCOO^-} = \frac{2F \times n_{HCOO^-}}{i_{total} \times t} \quad (5)$$

where t is the chronoamperometry time, then

$$j_{HCOO^-} = \frac{FE_{HCOO^-} \times i_{total}}{electrode\ area} \quad (6)$$

In-situ Raman spectra
In situ Raman cell was custom-made from GaossUnion, China. The carbon paper (Toray H90) loaded with catalyst was set in the bottom of the Raman cell as a working electrode. The reference electrode (Ag/AgCl) and a counter electrode (Pt wire) were purchased from GaossUnion, China. Before the experiments, the electrolyte (0.5 M KHCO₃) was saturated with CO_2 (80 mL min^{-1}, 30 min) at room temperature and ambient pressure. A laser confocal micro spectrometer (Renishaw inVia) with a 532 nm wavelength laser was used to obtain Raman spectroscopy. For the Bi-based catalyst, the scan range of the Raman shift was set at 50–500 cm^{-1}.

^{19}F-NMR
After a certain time of chronoamperometry test (CO_2 saturated 0.5 M KHCO₃, −0.97 V, glass carbon electrode), the catalyst was collected and used to quantify the fluorine content by ^{19}F-NMR spectra. The fluorine content of the catalyst was quantified by ^{19}F-NMR spectra. 150 mg samples (Bi_2O_3, Bi_2O_3-F) were dissolved by 300 μL D_2O and 300 μL HCl (30 wt%). After ultrasonication, the solution containing fluorine was collected by centrifugation for 10 mins (speed: 3300 g). Typical ^{19}F-NMR sample was mixed with 500 μL solution from centrifugation and 2 μL hexafluorobenzene (internal standard).

XPS characterization
For the ex-situ XPS characterization, the glassy carbon electrodes were used to investigate the dopant content variations during the electrochemical reactions[59,60]. To keep the original surface of the catalyst, the samples that underwent the electrochemical reactions were quickly held in a vacuum oven at 25°C until the beginning of XPS characterization.

DFT calculation
Density functional theory (DFT), as implemented in the plane-wave Vienna ab initio simulation package (VASP) code, was used for the theoretical calculations[61,62]. The standard projector augmented wave (PAW) method was used for characterizing interaction in valence electrons and ion core[63]. The exchange-correlation function was based on generalized gradient approximation as described by Perdew-Burke-Ernzerhof (GGA-PBE)[64]. The cut-off energy is set to 520 eV and the 1 eV width Gaussian smearing was used[65]. The first Brillouin zone integration adopted a Γ-centered Monkhorst-Pack k-point grid (resolution: 0.3 Å^{-1})[66]. For the correction of the van der Waals force in the calculated structure, Grimme's DFT-D3 correction with the BJ damping was used[67]. The convergence tolerances of 10^{-4} eV/atom for energy and 0.02 eV/Å for maximum force were used for the geometrical optimizations. The size of Bi slab (54 atoms) were 13.60500 Å (a-axis), 14.18690 Å (b-axis), and 21.75030 Å (c-axis) respectively, where the vacuum region in the c-axis was set to a space of 15 Å to eliminate interactions between the adjacent layers. The configuration of K-point was (3, 3, 1). The Gibbs free energy of the intermediates at zero potential is calculated by using $\Delta G = \Delta E + \Delta ZPE - T\Delta S$[42,68], where ΔE is the total energy difference. ΔZPE and $T\Delta S$ are zero-point energy correction and entropy change at room temperature (298.15 K). The computational detail for Pourbaix diagram was referred to by the previous literature[69]. The construction of a theoretical Pourbaix diagram implies deriving G(pH, U) or ΔG(pH, U) values for the possible surface structures for a broad range of pH and U. Applying an electrochemical-thermodynamic approach, the equation was as follows:

$$\Delta G(pH,U) = \Delta G(0,0) - v(H^+)k_B T(\ln 10)pH - v(e^-)eU$$

where e is the elementary charge of an electron and U is the applied electrode potential with respect to the SHE.

Data availability
Source data are provided with this paper.

References
1. Wu, J. et al. A metal-free electrocatalyst for carbon dioxide reduction to multi-carbon hydrocarbons and oxygenates. *Nat. Commun.* **7**, 13869 (2016).
2. Ni, W. et al. Fluorine doped cagelike carbon electrocatalyst: An insight into the structure-enhanced CO selectivity for CO_2 reduction at high overpotential. *ACS Nano* **14**, 2014–2023 (2020).
3. Ma, W. et al. Electrocatalytic reduction of CO_2 to ethylene and ethanol through hydrogen-assisted C–C coupling over fluorine-modified copper. *Nat. Catal.* **3**, 478–487 (2020).
4. Wang, X. et al. Efficient electrically powered CO_2-to-ethanol via suppression of deoxygenation. *Nat. Energy* **5**, 478–486 (2020).
5. Liu, S.-Q. et al. Electronic delocalization of bismuth oxide induced by Sulfur doping for efficient CO_2 electroreduction to formate. *ACS Catal.* **11**, 7604–7612 (2021).
6. Chen, S. et al. Molybdenum sulfide clusters-nitrogen-doped graphene hybrid hydrogel film as an efficient three-dimensional hydrogen evolution electrocatalyst. *Nano Energy* **11**, 11–18 (2015).
7. Qu, K. et al. Promotion of electrocatalytic hydrogen evolution reaction on Nitrogen-doped carbon nanosheets with secondary heteroatoms. *ACS Nano* **11**, 7293–7300 (2017).
8. Gong, K. et al. Nitrogen-doped carbon nanotube arrays with high electrocatalytic activity for oxygen reduction. *Science* **323**, 760–764 (2009).
9. Guo, D. et al. Active sites of nitrogen-doped carbon materials for oxygen reduction reaction clarified using model catalysts. *Science* **351**, 361–365 (2016).
10. Zhao, Y. et al. Few-layer graphdiyne doped with sp-hybridized nitrogen atoms at acetylenic sites for oxygen reduction electrocatalysis. *Nat. Chem.* **10**, 924–931 (2018).
11. Zhao, Y. et al. Nitrogen-doped carbon nanomaterials as non-metal electrocatalysts for water oxidation. *Nat. Commun.* **4**, 2390 (2013).

12. Mamtani, K. et al. Insights into oxygen reduction reaction (ORR) and oxygen evolution reaction (OER) active sites for nitrogen-doped carbon nanostructures (CNx) in acidic media. *Appl. Catal. B: Environ.* **220**, 88–97 (2018).

13. Wang, H. et al. Polymer-derived heteroatom-doped porous carbon materials. *Chem. Rev.* **120**, 9363–9419 (2020).

14. Cheng, H. et al. Surface nitrogen-injection engineering for high formation rate of CO_2 reduction to formate. *Nano Lett.* **20**, 6097–6103 (2020).

15. Liu, Y. et al. A highly efficient metal-free electrocatalyst of F-doped porous carbon toward N_2 electroreduction. *Adv. Mater.* **32**, 1907690 (2020).

16. Liu, X. et al. Carbon nanotubes with fluorine-rich surface as metal-free electrocatalyst for effective synthesis of urea from nitrate and CO_2. *Appl. Catal. B: Environ.* **316**, 121618 (2022).

17. Xie, J. et al. Metal-free fluorine-doped carbon electrocatalyst for CO_2 reduction outcompeting hydrogen evolution. *Angew. Chem. Int. Ed.* **57**, 9640–9644 (2018).

18. Yang, X. et al. Partial sulfuration-induced defect and interface tailoring on bismuth oxide for promoting electrocatalytic CO_2. *Reduct. J. Mater. Chem. A* **8**, 2472–2480 (2020).

19. Li, J. et al. Graphitic-N highly doped graphene-like carbon: a superior metal-free catalyst for efficient reduction of CO_2. *Appl. Catal. B: Environ.* **298**, 120510 (2021).

20. Zeng, Q. et al. Effects of nitrogen and oxygen on electrochemical reduction of CO_2 in nitrogen-doped carbon black. *Carbon* **202**, 1–11 (2023).

21. Wu, C. et al. NiFe layered double hydroxides with unsaturated metal sites via precovered surface strategy for oxygen evolution reaction. *ACS Catal.* **10**, 11127–11135 (2020).

22. Bhatnagar, A. et al. Fluoride removal from water by adsorption—a review. *Chem. Eng. J.* **171**, 811–840 (2011).

23. Zhang, B. et al. Fluoride-induced dynamic surface self-reconstruction produces unexpectedly efficient oxygen-evolution catalyst. *Nano Lett.* **19**, 530–537 (2019).

24. Zhu, C. et al. Highly efficient nonprecious metal catalysts towards oxygen reduction reaction based on three-dimensional porous carbon nanostructures. *Chem. Soc. Rev.* **45**, 517–531 (2016).

25. Kulkarni, A. et al. Understanding catalytic activity trends in the oxygen reduction reaction. *Chem. Rev.* **118**, 2302–2312 (2018).

26. Hu, C. et al. Carbon-based metal-free electrocatalysts: from oxygen reduction to multifunctional electrocatalysis. *Chem. Soc. Rev.* **50**, 11785–11843 (2021).

27. Feng, X. et al. Untangling the respective effects of heteroatom-doped carbon materials in batteries, supercapacitors and the ORR to design high performance materials. *Energy Environ. Sci.* **14**, 2036–2089 (2021).

28. Liu, C. et al. Tuning strategies and structure effects of electrocatalysts for carbon dioxide reduction reaction. *Chin. J. Catal.* **43**, 1618–1633 (2022).

29. Cheon, J. Y. et al. Intrinsic relationship between enhanced oxygen reduction reaction activity and nanoscale work function of doped carbons. *J. Am. Chem. Soc.* **136**, 8875–8878 (2014).

30. Lin, Y. et al. Tuning charge distribution of FeN_4 via external N for enhanced oxygen reduction reaction. *ACS Catal.* **11**, 6304–6315 (2021).

31. Xia, B. Y. et al. A metal–organic framework-derived bifunctional oxygen electrocatalyst. *Nat. Energy* **1**, 15006 (2016).

32. He, B. et al. Boron-doped C_3N monolayer as a promising metal-free oxygen reduction reaction catalyst: A theoretical insight. *J. Phys. Chem. C.* **122**, 20312–20322 (2018).

33. Tao, L. et al. Bridging the surface charge and catalytic activity of a defective carbon electrocatalyst. *Angew. Chem. Int. Ed.* **58**, 1019–1024 (2019).

34. Zhu, J. & Mu, S. Defect engineering in carbon-based electrocatalysts: Insight into intrinsic carbon defects. *Adv. Funct. Mater.* **30**, 2001097 (2020).

35. Ko, Y.-J. et al. Exploring dopant effects in stannic oxide nanoparticles for CO_2 electro-reduction to formate. *Nat. Commun.* **13**, 2205 (2022).

36. Zheng, W. et al. Accelerating industrial-level CO_2 electroreduction kinetics on isolated zinc centers via sulfur-boosted bicarbonate dissociation. *Energy Environ. Sci.* **16**, 1007–1015 (2023).

37. Wang, Y. et al. Lattice-dislocated Bi nanosheets for electrocatalytic reduction of carbon dioxide to formate over a wide potential window. *J. Colloid Interface Sci.* **611**, 246–254 (2022).

38. Prasad, N. & Balasubramanian, K. Raman spectral probe on increased local vibrational modes and phonon lifetimes in Ho^{3+}-doped Bi_2O_3 micro-rods. *J. Raman Spectrosc.* **47**, 1266–1270 (2016).

39. Hardcastle, F. D. & Wachs, I. E. The molecular structure of bismuth oxide by Raman spectroscopy. *J. Solid State Chem.* **97**, 319–331 (1992).

40. Toby, B. H. & Von Dreele, R. B. GSAS-II: the genesis of a modern open-source all purpose crystallography software package. *J. Appl. Crystallogr.* **46**, 544–549 (2013).

41. Becke, A. D. & Edgecombe, K. E. A simple measure of electron localization in atomic and molecular systems. *J. Chem. Phys.* **92**, 5397–5403 (1990).

42. Peterson, A. A. & Nørskov, J. K. Activity descriptors for CO_2 electroreduction to methane on transition-metal catalysts. *J. Phys. Chem. Lett.* **3**, 251–258 (2012).

43. Han, N. et al. Ultrathin bismuth nanosheets from in situ topotactic transformation for selective electrocatalytic CO_2 reduction to formate. *Nat. Commun.* **9**, 1320 (2018).

44. Gong, Q. et al. Structural defects on converted bismuth oxide nanotubes enable highly active electrocatalysis of carbon dioxide reduction. *Nat. Commun.* **10**, 2807 (2019).

45. Yang, F. et al. Bismuthene for highly efficient carbon dioxide electroreduction reaction. *Nat. Commun.* **11**, 1088 (2020).

46. Wang, X. et al. Heteroatom-doped graphene materials: syntheses, properties and applications. *Chem. Soc. Rev.* **43**, 7067–7098 (2014).

47. Wei, P. et al. Porous N, B co-doped carbon nanotubes as efficient metal-free electrocatalysts for ORR and Zn-air batteries. *Chem. Eng. J.* **422**, 130134 (2021).

48. Gao, K. et al. Efficient metal-free electrocatalysts from N-doped carbon nanomaterials: Mono-doping and Co-doping. *Adv. Mater.* **31**, 1805121 (2019).

49. Liu, J. et al. High performance platinum single atom electrocatalyst for oxygen reduction reaction. *Nat. Commun.* **8**, 15938 (2017).

50. Liu, J. et al. High-performance oxygen reduction electrocatalysts based on cheap carbon black, nitrogen, and trace iron. *Adv. Mater.* **25**, 6879–6883 (2013).

51. Cachet, H. et al. Corrosion-induced activation of SnO_2 films promoted by the electrochemical oxidation of chloride ions. *J. Electrochem. Soc.* **146**, 977 (1999).

52. Kim, J. M. et al. High-performance corrosion-resistant fluorine-doped tin oxide as an alternative to carbon support in electrodes for PEM fuel cells. *Nano Energy* **65**, 104008 (2019).

53. Fan, L. et al. CO_2/carbonate-mediated electrochemical water oxidation to hydrogen peroxide. *Nat. Commun.* **13**, 2668 (2022).

54. Geiger, S. et al. Stability limits of tin-based electrocatalyst supports. *Sci. Rep.* **7**, 4595 (2017).

55. Quin, P. et al. Lowering N_2O emissions from soils using eucalypt biochar: the importance of redox reactions. *Sci. Rep.* **5**, 16773 (2015).

56. Gunasooriya, G. T. K. K. & Nørskov, J. K. Analysis of acid-stable and active oxides for the oxygen evolution reaction. *ACS Energy Lett.* **5**, 3778–3787 (2020).

57. Shi, J. et al. Eliminating trap-states and functionalizing vacancies in 2D semiconductors by electrochemistry. *Small* **15**, 1901899 (2019).

58. Oh, H.-S. et al. Preparation of mesoporous Sb-, F-, and In-doped SnO$_2$ bulk powder with high surface area for use as catalyst supports in electrolytic cells. *Adv. Funct. Mater.* **25**, 1074–1081 (2015).

59. Wu, Y. et al. Electrochemical palladium-catalyzed oxidative sonogashira carbonylation of arylhydrazines and alkynes to ynones. *J. Am. Chem. Soc.* **143**, 12460–12466 (2021).

60. Badalyan, A. & Stahl, S. S. Cooperative electrocatalytic alcohol oxidation with electron-proton-transfer mediators. *Nature* **535**, 406–410 (2016).

61. Kresse, G. & Furthmüller, J. Efficient iterative schemes for ab initio total-energy calculations using a plane-wave basis set. *Phys. Rev. B* **54**, 11169–11186 (1996).

62. Kresse, G. & Furthmüller, J. Efficiency of ab-initio total energy calculations for metals and semiconductors using a plane-wave basis set. *Computational Mater. Sci.* **6**, 15–50 (1996).

63. Blöchl, P. E. Projector augmented-wave method. *Phys. Rev. B* **50**, 17953–17979 (1994).

64. Perdew, J. P. et al. Generalized gradient approximation made simple. *Phys. Rev. Lett.* **78**, 1396–1396 (1997).

65. Methfessel, M. & Paxton, A. T. High-precision sampling for Brillouin-zone integration in metals. *Phys. Rev. B* **40**, 3616–3621 (1989).

66. Pack, J. D. & Monkhorst, H. J. "Special points for Brillouin-zone integrations"–a reply. *Phys. Rev. B* **16**, 1748–1749 (1977).

67. Grimme, S. Semiempirical GGA-type density functional constructed with a long-range dispersion correction. *J. Comput. Chem.* **27**, 1787–1799 (2006).

68. Nørskov, J. K. et al. Origin of the overpotential for oxygen reduction at a fuel-cell cathode. *J. Phys. Chem. B* **108**, 17886–17892 (2004).

69. Hansen, H. A. et al. Surface pourbaix diagrams and oxygen reduction activity of Pt, Ag and Ni(111) surfaces studied by DFT. *Phys. Chem. Chem. Phys.* **10**, 3722–3730 (2008).

Acknowledgements

Author contributions

W.Xu. designed the idea. C.L. performed the material synthesis, characterization, experiments, and data analysis. B.M. and Z.J. performed X-ray absorption spectra (XAS) analysis. Z.S., J.G., W.Xing performed in-situ Raman analysis. P.S. performed DFT calculations. C.L., P.S., and W.Xu wrote the original draft. All authors reviewed and edited the manuscript.

Competing interests

The authors declare no competing interests.

Additional information

Supplementary information The online version contains supplementary material available at https://doi.org/10.1038/s41467-023-44480-9.

Correspondence and requests for materials should be addressed to Ping Song or Weilin Xu.

Peer review information *Nature Communications* thanks Dong Liu, Jong Min Kim and the other, anonymous, reviewer(s) for their contribution to the peer review of this work. A peer review file is available.

Reprints and permissions information is available at http://www.nature.com/reprints

Publisher's note Springer Nature remains neutral with regard to jurisdictional claims in published maps and institutional affiliations.